Supporting information for:

Excited-State Dynamics and Photochromism of Extended Tetraphenylethylene Derivatives and Their Control by Amino Conjugation Effect

Mathilde Seinfeld,*[a] Xingjie Fu,[b] Tangui le Bahers,*[a,c] Chantal Andraud,[a] Stefan Haacke*,[b] Jean Rouillon*,[a] and Cyrille Monnereau*[a]

a. Univ Lyon, Ecole Normale Supérieure de Lyon, Laboratoire de Chimie, CNRS UMR 5182, 69342 Lyon, France

b. Institut de Physique et Chimie des Matériaux de Strasbourg, Université de Strasbourg, CNRS UMR 7504 Strasbourg, France

c. Institut Universitaire de France, 5 rue Descartes, 75005 Paris, France

*corresponding authors: mathilde.seinfeld@ens-lyon.fr, tangui.le_bahers@ens-lyon.fr, jean.rouillon@laposte.net, stefan.haacke@ipcms.unistra.fr, cyrille.monnereau@ens-lyon.fr

Table of content

Synthesis

Synthesis of **TPE-TPA** was depicted in reference 1, TPE-OMe and TPE-F in reference 2. TPE was ordered from TCI Europe (98% puriss) and used as received

Photoisomerization quantum yield determination

- ^{1}H NMR spectra were recorded at room temperature on a Bruker Avance 400 spectrometer operating at 400 MHz. $CDCl_3$ (d, 99.8%) was purchased from Euroisotop. Chemical shifts are given as values (ppm) referenced to the peak of $CDCl_3$ (7.26 ppm). All experiments were performed in quartz NMR tubes. The accuracy of the NMR integrations in the titration conditions was checked by comparing the integrations obtained on a test sample acquired with a relaxation time T1 corresponding to those used in the standard titration experiments, T1 being acquired with approximately five times longer relaxation delays. The measured integrations remained unchanged. NMR integrations and peak heights were estimated using MestReNova. Exponential fitting, tangent and exact method treatment of the obtained data were performed using Origin software.

- The irradiation source was the 450 W xenon arc lamp of a Horiba Jobin-Yvon Fluorolog-3 spectrofluorimeter, and the irradiation wavelength was selected using an iHR320 excitation monochromator with 1200 groves.mm^{-1} grating. Irradiation experiments were performed in a calibrated integrative sphere (2π steradian covered with spectralon®, model G8 from GMP). The value of incident photon flux used were determined by chemical actinometry based on the photoconversion of 2-nitrobenzaldehyde to 2-nitrosobenzoic acid.[2] Values obtained accordingly are given in Table S1.

Table S1. Light intensities and maximum wavelength used for irradiation of **TPE-TPA**

	TPE-TPA
I_0 (s^{-1})	9.48×10^{15}
λ (nm)	372

- The irradiation of NMR tube in an integrating sphere is fully described in a previous paper.[2] The accuracy of the method was verified by comparing this setup with conventional irradiation in a spectroscopic cuvette under constant agitation, with deviations in incident power measurements of less than 3%. The ratio of photons absorbed by the contents of the NMR tube in the integration sphere to the incident photon flux was estimated by integrating the excitation spectra of the lamp in the absence and presence of the sample. Stock solutions in $CDCl_3$ were prepared at specific concentrations using volumetric flasks. The solutions were transferred to the NMR tube. Irradiation was started at t = 0, ^{1}H spectra were recorded at precise intervals of irradiation time and the conversion was calculated from the respective integrations of reactant and product(s). The center of the multiplet at 7.13 ppm was chosen to follow the evolution of the proportion of E isomer and the center of the multiplet at 7.11 ppm for the Z isomer.

- Two methodologies were employed to determine the photoisomerization quantum yields φ_{iso} (Photoisomerization of the (Z)-isomer has been chosen for illustration in the following formula; similar logic applies to the (E)-isomer).

  (i) Extrapolation method: the kinetic constant k_{iso} associated to the (Z) → (E) photoisomerization is estimated at the beginning of the reaction at t = 0.[3] At this stage, the (E)-isomer being in negligible concentration in the reaction mixture, the constant k_{iso} can be readily obtained according to equation S1:

$$\lim_{([Z]-[Z]_0)\to 0} \frac{[Z]_0-[Z]}{t} = k_{iso} \quad \text{(S1)}$$

Photoisomerization quantum yield can be derived from the measured k_{iso} according to equation S2:

$$\Phi_{iso} = \frac{k_{iso}.N_A.V}{I_{abs}} \quad \text{(S2)}$$

With k_{iso} is the kinetic constant of the photoisomerization (mol.L^{-1} .s^{-1}), N_A, the Avogadro constant, V, the volume of the solution (L), and I_{abs}, the absorbed photon flux (s^{-1}). Real amount I_{abs} of photon flux absorbed by the NMR tube in the integration sphere can be calculated following equation:

$$I_{abs} = I_0\left(1 - \frac{L_c}{L_a}\right) \quad \text{(S3)}$$

With I_0 corresponds to the incident photon flux, L_c and L_a are the integrated excitation spectra of the sphere (i.e. measured signal of the light source) with and without the sample NMR tube respectively.

(ii) Exact method: this consists in obtaining a pair of solutions to the differential equation S4, describing the entire process of photoisomerization [4] by using regression algorithms applied to non-linear multivariate functions. Bayda et al. propose to apply the Levenberg-Marquardt algorithm to an exponential form of the solution:[4]

$$exp\left(-\frac{t}{s}\right) = exp\left(\frac{\varepsilon_Z - \varepsilon_E}{I_{abs}(z+e)}\frac{[Z]-[Z]_0}{s}\right) \times \left(1 + \frac{1}{[Z]_0}\left(1 + \frac{e}{z}\right)([Z] - [Z]_0)\right)^{\frac{[Z]_0\ z\varepsilon_E + e\varepsilon_Z}{s\ I_{abs}(z+e)^2}} \quad \text{(S4)}$$

With $[Z]_0$, the initial concentration of the (Z)-isomer, $z = \varepsilon_Z\Phi_{Z\rightarrow E}$, $e = \varepsilon_E\Phi_{E\rightarrow Z}$, and s, a scale factor.

By applying the fitting algorithm to the curve of exp(- ts) versus [Z] - $[Z]_0$ (equation S4), a pair of solutions (z,e) is calculated. This method thus makes it possible to obtain the two quantum yields of photoisomerization with the study of a single kinetic and by applying it to the whole reaction.

Parameters and quantum yields deduced by both methods are summarized in Table S2. For photoisomerization kinetics, χ^2 test of the exponential fit with the constant k_{iso} extrapolated from the tangent at zero-time are presented. For the exact method, χ^2 test of the fit to equation S4 with the obtained photoisomerization quantum yield Φ_1 and Φ_2 are included in the corresponding graphs. In all cases, good consistencies were found when comparing the yields obtained by both methods.

Table S2. Summary of the parameters and yields of photoisomerization obtained for ***E*** and ***Z*** **TPE-TPA**.

	***Z*-TPE-TPA**	***E*-TPE-TPA**
k_{iso} (mol.L^{-1}.s^{-1})	2.33x10^{-6}	1.98x10^{-6}
V (L)	5.00x10^{-4}	5.00x10^{-4}
L_a	6.85x10^{7}	6.72x10^{7}
L_c	1.36x10^{6}	1.25x10^{6}
1-(L_c/L_a)	0.802	0.812
Φ_{iso} (extrapolation)	0.09	0.08
χ^2 (extrapolation)	0.984	0.999
Φ_{iso} (exact method)	0.10	0.08
χ^2 (exact method)	0.965	0.998

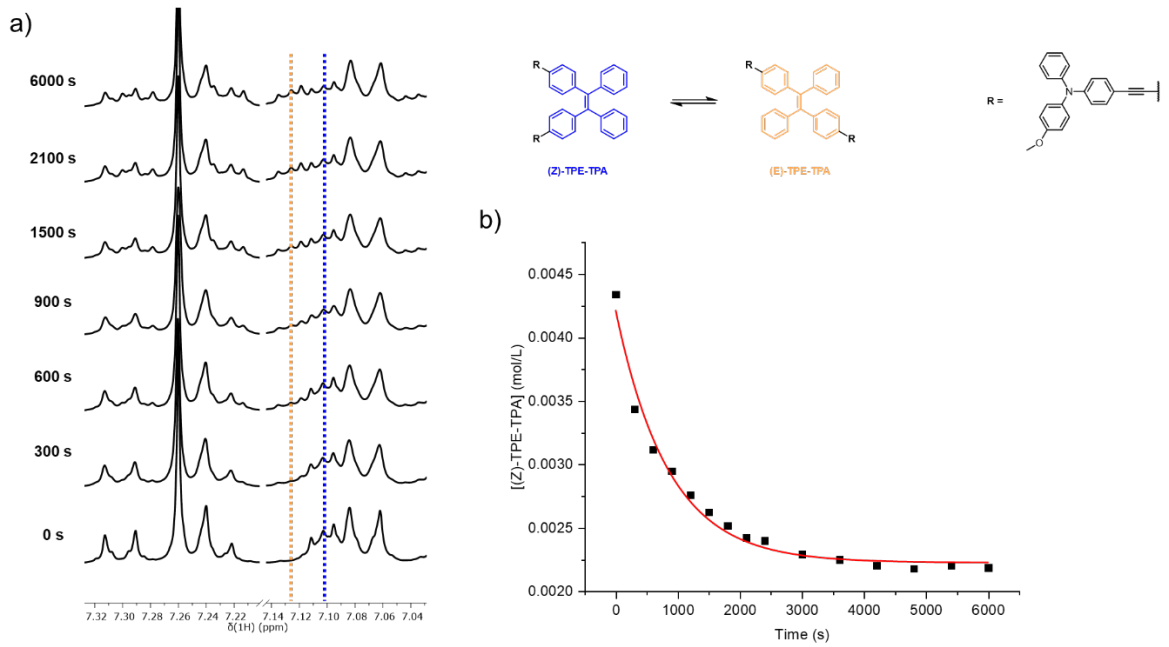

Fig. S1 (a) Close-up view on aromatic region of ^{1}H NMR spectra during irradiation of ***Z*-TPE-TPA** (in solution of $CDCl_3$, at room temperature, with a spectrometer operating at 400 MHz). (b) Photoisomerization kinetic of ***Z*-TPE-TPA** in solution (Red curve corresponding to exponential fit).

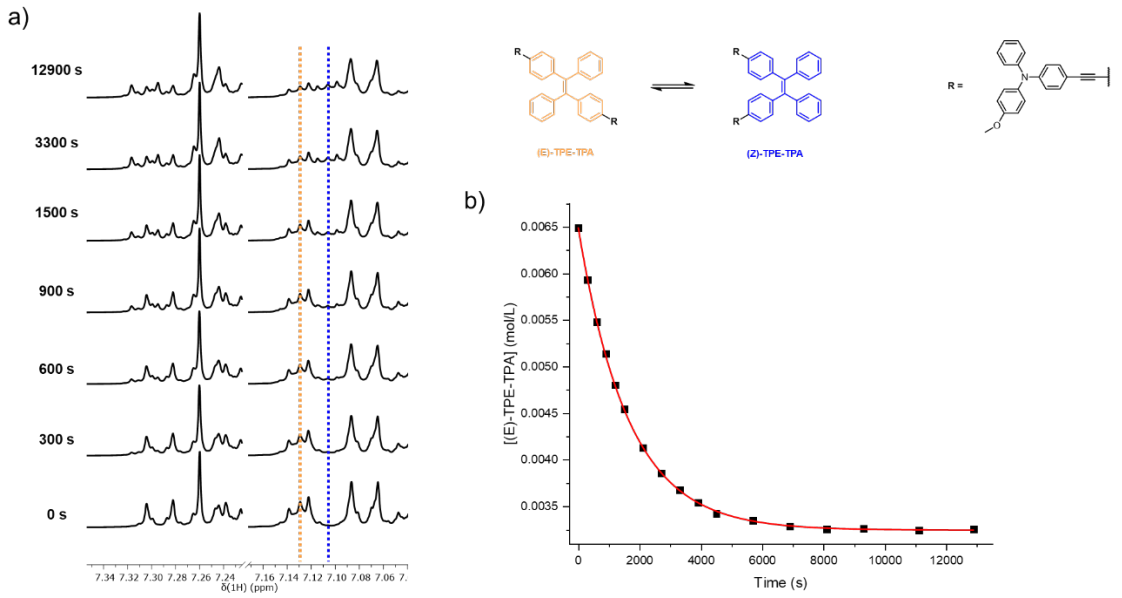

Fig. S2 (a) Close-up view on aromatic region of ^{1}H NMR spectra during irradiation of ***E*-TPE-TPA** (in solution of $CDCl_3$, at room temperature, with a spectrometer operating at 400 MHz). (b) Photoisomerization kinetic of ***E*-TPE-TPA** in solution (Red curve corresponding to exponential fit).

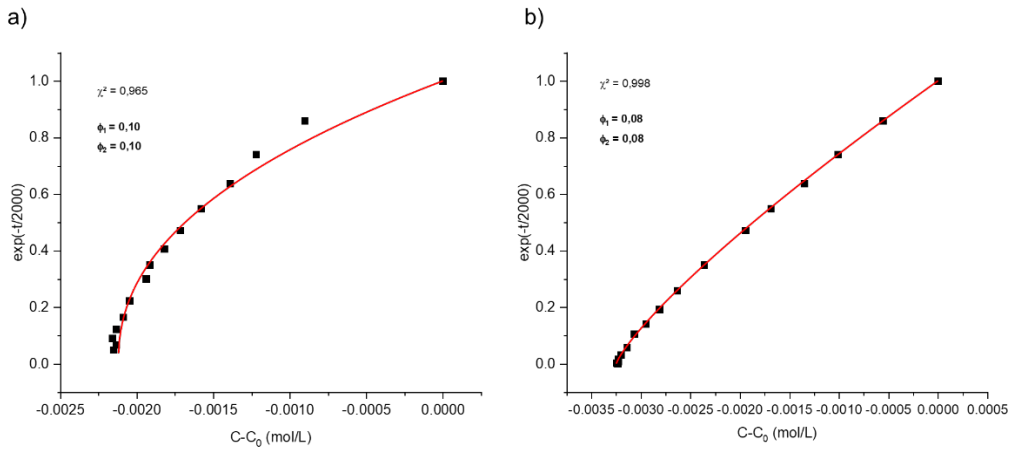

Fig. S3 Exact method treatment of photoisomerization kinetics of (a) ***Z*-TPE-TPA** and (b) ***E*-TPE-TPA** (Red curve corresponding to the fit to equation S4).

Table S3. Ratios of ***Z*-TPE-TPA** calculated by ^{1}H-NMR during irradiation

Time (s)	Intensity (a.u.)		*Z*-isomer ratio
	E-Peak	*Z*-Peak	
0	-	-	1.000
300	128.2	589.4	0.792
600	170.4	526.1	0.719
900	198.7	508.9	0.679
1200	242.4	512.1	0.636
1500	264.6	489.1	0.604
1800	284.9	477.2	0.581
2100	309	472.7	0.558
2400	297.5	445.2	0.553
3000	335.5	454.6	0.528
3600	336.3	438.1	0.519
4200	346.6	433	0.508
4800	363.1	443.7	0.503
5400	328	409.3	0.508
6000	340.2	418.1	0.504

Table S4. Ratios of ***E*-TPE-TPA** calculated by ^{1}H-NMR during irradiation.

Time (s)	Intensity (a.u.)		*E*-isomer ratio
	E-Peak	*Z*-Peak	
0	-	-	1.000
300	1000	183.7	0.914
600	928.9	262.1	0.844
900	887.1	325.4	0.792
1200	806.2	373.1	0.740
1500	781.1	426.4	0.700
2100	693.9	487.2	0.636
2700	639.3	524.7	0.594
3300	626.4	570.8	0.566
3900	596.4	587.2	0.545
4500	545.3	574.3	0.527
5700	566	620.8	0.516
6900	538.7	612.8	0.506
8100	526.9	608.9	0.502
9300	540.7	623.3	0.503
11100	536.4	624.3	0.500
12900	544.4	630.4	0.502

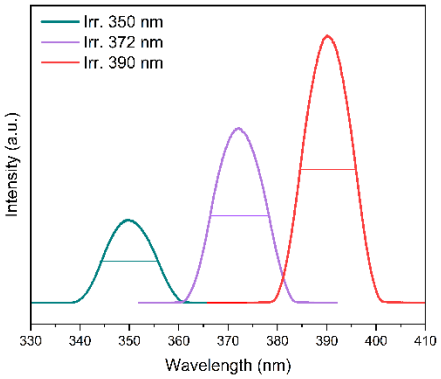

Figure S4: Spectral profil of the irradiation sources used for the isomerization experiments. The full width at half maximum of each peak is highlighted and measured at 12 nm for all peaks.

Comparison of the spectroscopic properties of the *E* and *Z* forms of other stereopure TPE derivatives reported in previous literature, and associated references.

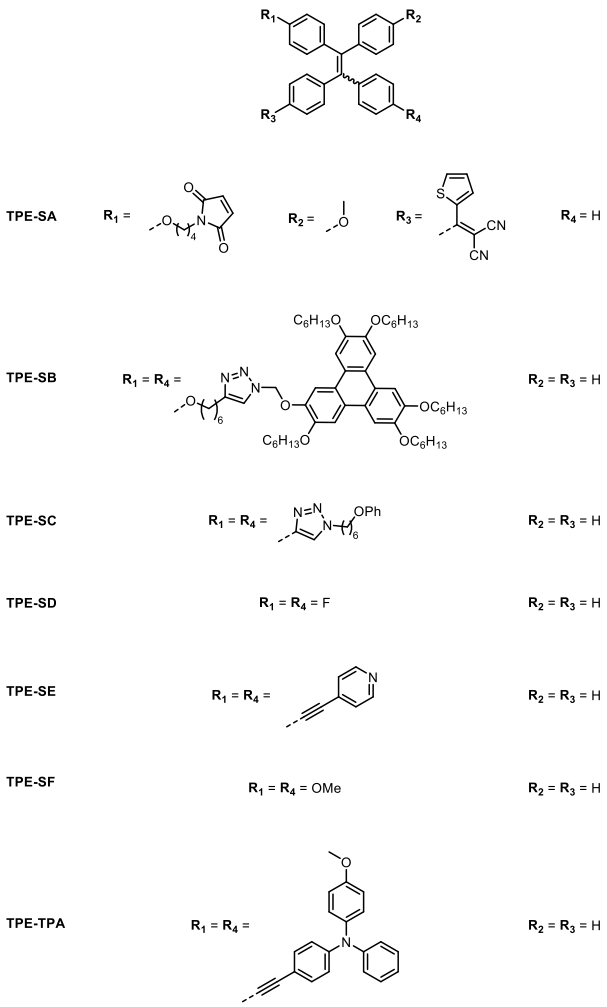

Table S5. Absorption differences between *E* and *Z* isomers of stereopures TPE derivatives already described in the literature (only some illustrating examples in case of no spectral differences).

Compound	Absorption of *E*-isomer (nm)	Absorption of *Z*-isomer (nm)	absorption difference E-Z (cm^{-1})	Solvent	Ref.
TPE-SA	440	440	0	DMSO	[5]
TPE-SB	290	290	0	THF	[6]
TPE-SC	332	332	0	THF	[7]
TPE-SD	304	305	108	THF	[8]
TPE-SE	345	347	167	EtOH	[9]
TPE-SF	322	320	194	THF	[8]
TPE-TPA	370	361	674	THF	[1]

Steady-state Spectroscopy

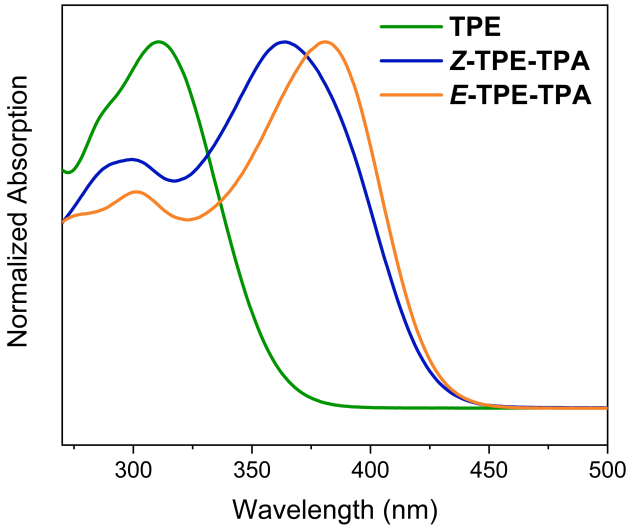

Figure S5: Steady-state absorption spectra of **TPE** (green), ***E*-TPE-TPA** (yellow) and ***Z*-TPE-TPA** (blue) in CH_2Cl_2.

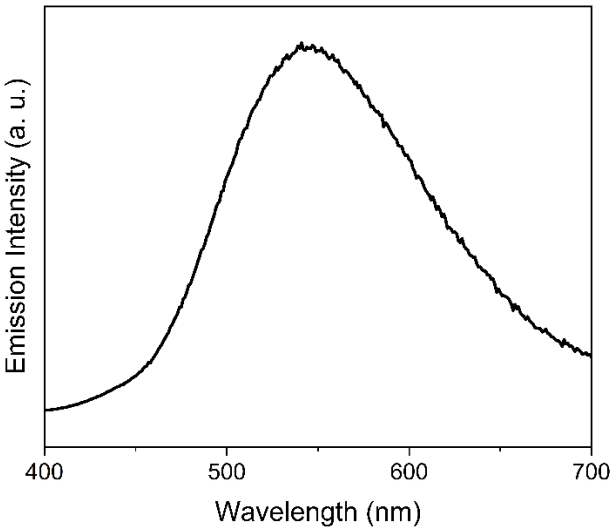

Figure S6: Steady-state emission spectra of **TPE-TPA** in CH_2Cl_2.

Time-resolved Spectroscopy

1. Transient Absorption Spectroscopy (TAS)

The femto-second transient absorption spectroscopy was performed on a home-built pump-probe setup[14]. The setup operates on 800 nm mode-locked laser from Ti: sapphire oscillator (Femtolasers Produktions GmbH) at a repetition rate of 5 kHz. The pulse width of the 800 nm laser is compressed to 40 fs by the action of a compressor (Amplitude Technologies). A beam splitter disproportionally divides the 800 nm beam into a weak beam (10% of the energy) and a strong beam (90% of the energy). The weak beam passes through a delay stage (0 to 5 ns range) and is focused on a non-linear crystal to generate a broadband supercontinuum as the probe beam. To cover a probing spectral range spanning from UV to NIR, both CaF2 and sapphire of 2 mm thickness are used as the non-linear crystal. The strong beam is redirected into an optical parametric amplifier (TOPAS, Light Conversion) to generate a NIR beam of 1280 nm, and the final 320 nm pump beam is obtained via two consecutive frequency

doubling processes. The pump beam and the probe beam spatially overlap in a 0.5 mm quartz flow cell. The linear polarization of the pump beam is set to be at magic angle (54.7 °) to that of the probe beam. Two synchronized mechanic shutters, one operating at 114 Hz and the other at 227 Hz, are installed on the pump beam path before the sample and in front of the detection module (Jobin Yvon H 25 + Princeton Instruments 7500-0001) respectively, which enables the automatic data acquisition of the differential absorbance. To subtract the solvent contribution of the TAS signal, i.e., the pump-probe cross-phase modulation, the two-photon absorption and the stimulated Raman amplification, for each TAS measurement an additional measurement of the solvent under the same experimental condition is performed. Lastly, the clear solvent signal is also used to define the correction function for the group velocity dispersion of the supercontinuum over the probing spectral range.

2. Femto-second Fluorescence Up-Conversion Spectroscopy (FLUPS)

The femto-second fluorescence up-conversion spectroscopy uses the same 5 kHz 800 nm fundamental laser from Ti: sapphire system described above for the TAS setup. The detailed description of the FLUPS setup has been given in previous work[15,16]. A 1280 nm gate beam and a 320 nm pump are generated via the optical parametric amplifier (TOPAS, Light Conversion) from the 800 nm fundamental laser. The pump beam is focused onto a 0.2 mm flow cell to excite the sample. The excitation volume of the focused pump beam inside the flow cell is imaged into a 0.2 mm β-BBO crystal via two parabolic mirrors. The gate beam passes through a delay stage (0 to 3 ns range) and is focused into the β-BBO to spatially overlap with the fluorescence image of the focused pump beam. The β-BBO is mounted in a type II phase-matching configuration to generate the sum frequency signal of the gate beam and the fluorescence. In the type II phase-matching configuration, the gate beam is horizontally polarized, and the polarization of the pump beam is set to be at magic angle (54.7 °) to the vertical axis. The detection module of the sum frequency signal consists of a spectrograph (Action SpectraPro SP-2300, Princeton Instrument) and a nitrogen-cooled CCD camera (PyLoN, Princeton Instrument) kept at -80 ℃.

To calibrate the FLUPS spectrum signal intensity over the detection wavelength range, a blue-emitting fluorescence dye BBOT is used as the reference. The detailed procedure has been given elsewhere[17]. Briefly, a photometric calibration curve over the detection wavelength range is calculated as the intensity ratio between the normalized steady-state emission spectrum and the normalized wavelength-converted sum frequency spectrum at 200 ps delay of BBOT. At 200 ps delay, the nonadiabatic processes on the excited state has finished, and the transient emission spectrum of BBOT should share the same shape with its steady-state emission spectrum. Therefore, the calibration curve represents the distortion of the real emission signal due to the setup artifacts, including the filters, the wavelength-dependence of the detector, and the wavelength-dependence of the type II sum frequency generation process.

3. Data analysis for ultrafast spectroscopy

Both the TAS and the FLUPS measurements generate 2D data matrices of delay time and wavelength. The analysis of the kinetics is based on the multi-exponential decay model convoluted with a Gaussian instrument response function (IRF). The kinetic trace could be thus modelled as:

$$F(t) = A_0 + \sum_i \left\{ \frac{A_i}{2} exp\left(\frac{\sigma^2}{2\tau_i^2}\right) exp\left(-\frac{t-t_0}{\tau_i}\right) \left[1 + \boldsymbol{erf}\left(\frac{t-t_0-{\sigma^2}/{\tau_i}}{\sigma\sqrt{2}}\right)\right] \right\} + B\ exp\left(-\frac{(t-){t_0}^2}{2\sigma^2}\right)$$

where σ is the standard deviation of the Gaussian IRF, t_0 is the starting time of any action in the kinetic trace, τ_i is the lifetime of the ith exponential component, A_i is the amplitude of the ith exponential function, A_0 is the offset and B is the amplitude of the non-resolved sub time resolution kinetic component represented by a Gaussian function. To perform the non-linear multivariable curve-fitting, the variable projection (VARPRO) algorithm is implemented[18,19].

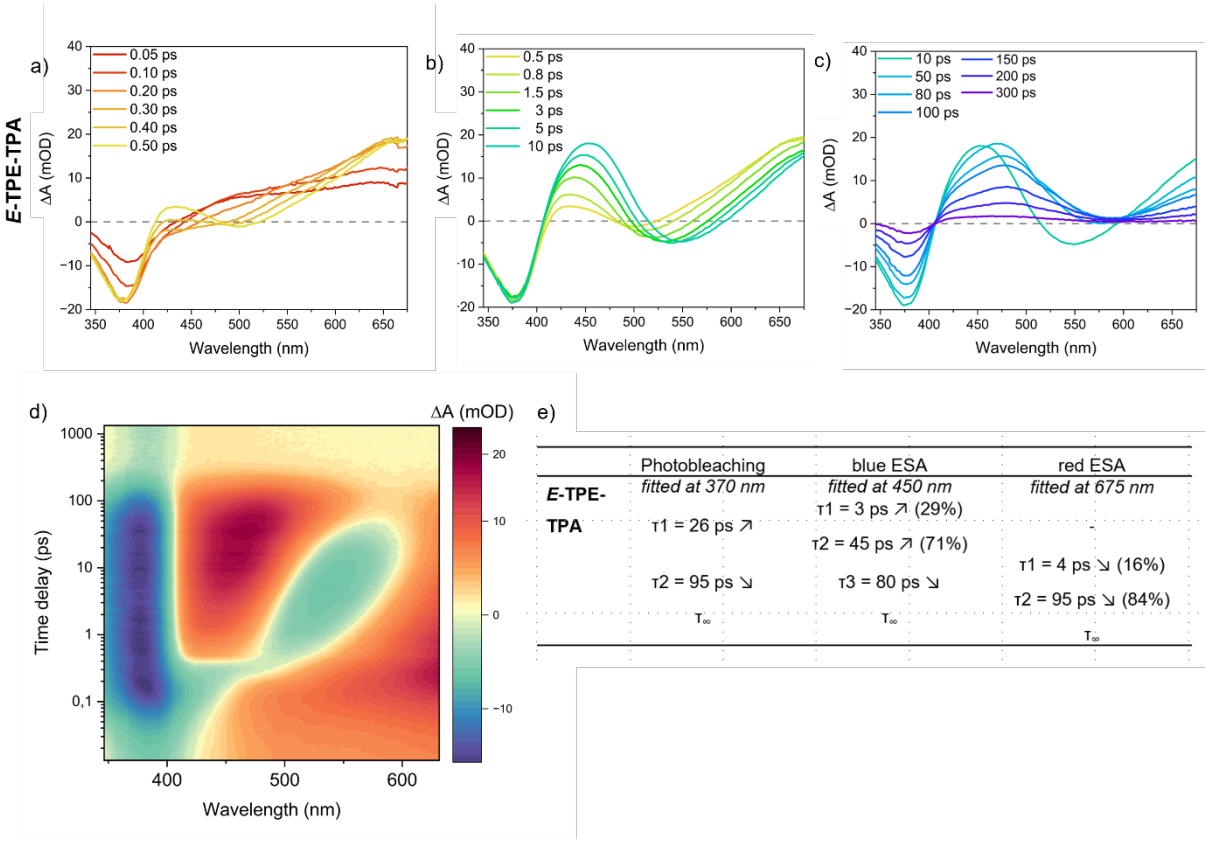

	Photobleaching	blue ESA	red ESA
	fitted at 370 nm	*fitted at 450 nm*	*fitted at 675 nm*
***E*-TPE-TPA**	τ1 = 26 ps ↗	τ1 = 3 ps ↗ (29%) τ2 = 45 ps ↗ (71%)	-
	τ2 = 95 ps ↘	τ3 = 80 ps ↘	τ1 = 4 ps ↘ (16%) τ2 = 95 ps ↘ (84%)
	τ_∞	τ_∞	τ_∞

Figure S7: Transient absorption spectroscopy (TAS) of ***E*-TPE-TPA** (right column) in CH_2Cl_2; d) 2D maps representing the TA data (ΔA coded in false color) as a function of probe wavelength (nm) and pump–probe time delay recorded; e) Table of the time constants τ (in ps) for ***E*-TPE-TPA** from TAS by fitting a kinetic trace at given wavelength (Fig. S10). Upward pointing arrow indicates a build-up of the state, downward pointing arrow a decay.

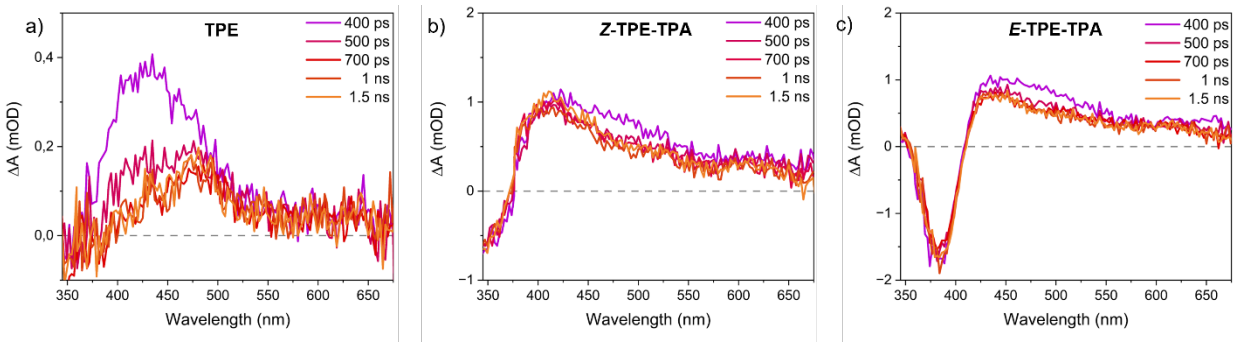

Figure S8: Transient absorption spectroscopy (TAS) of **TPE** (a), ***Z*-TPE-TPA** (b) and ***E*-TPE-TPA** (c) in CH_2Cl_2 at long delay time

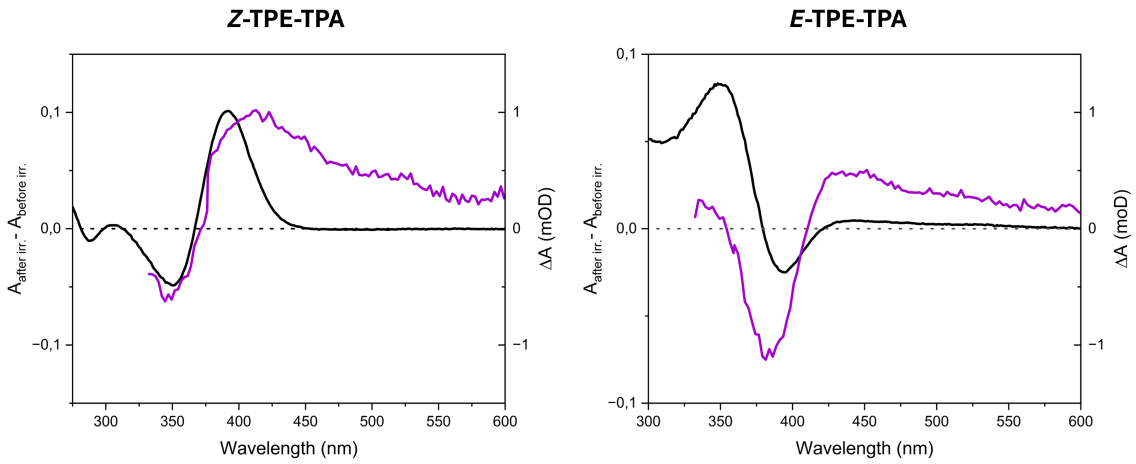

Figure S9: Difference of absorption spectrum from ***Z*-TPE-TPA** (left) or ***E*-TPE-TPA** (right) sample before and after TAS measurement in black, superposed with spectra of differential absorption (ΔA) at long delay time (> 1 ns) measured after respective TAS experiment in violet.

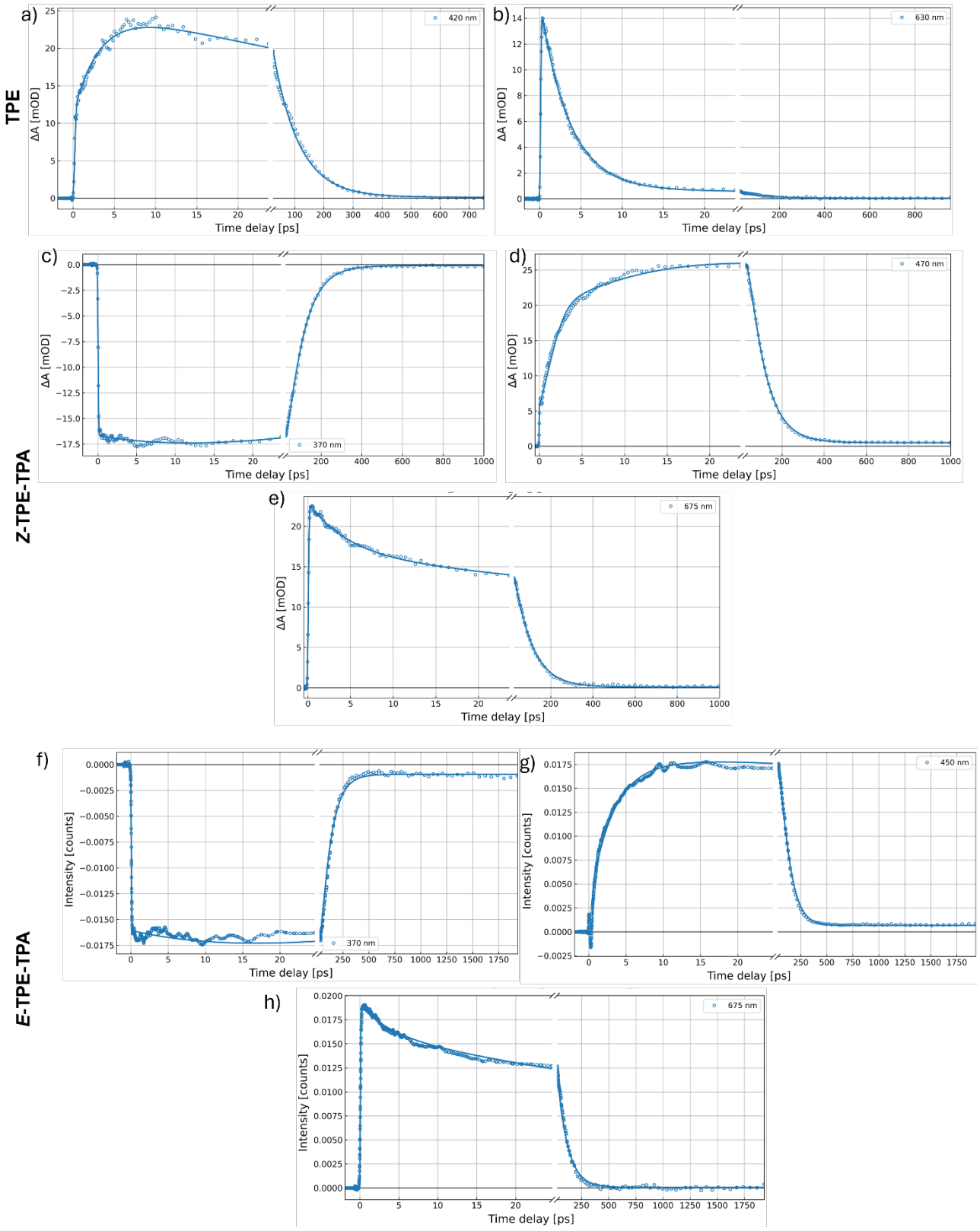

Figure S10: Decay kinetics for **TPE** (a, b), ***Z*-TPE-TPA** (c, d, e) and ***E*-TPE-TPA** at representative wavelength for ESA and photobleaching bands.

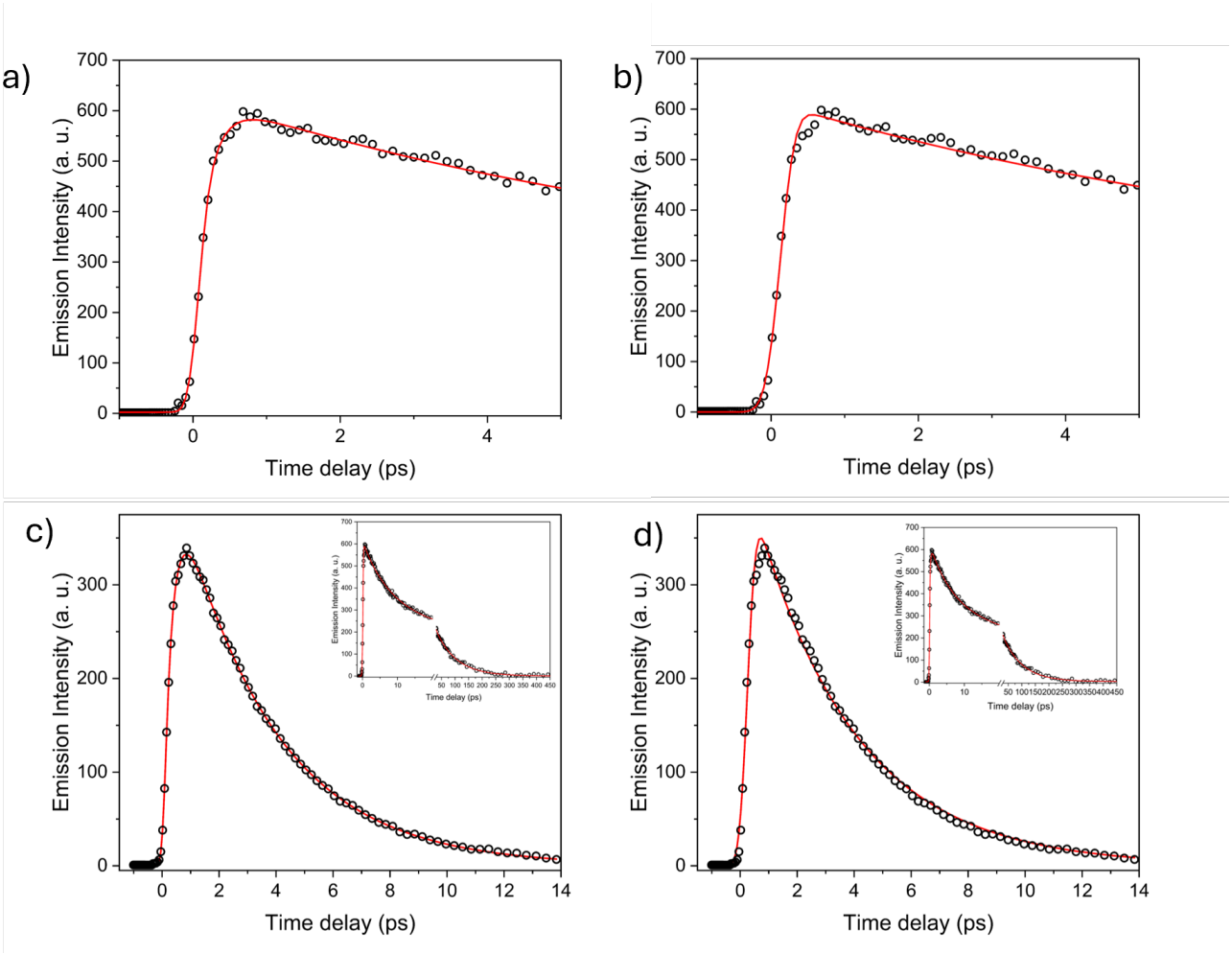

Figure S11: Comparison of the decay kinetics with a rising component (a, c) and without (b, d) for **TPE** (first row) and ***Z*-TPE-TPA** (second row, zoom on the first 14 ps, inset: global fit).

Computational details

Molecular calculations were performed with ORCA 5.0.4 software[10]. All geometries were optimized using DFT or TDA TD-DFT with the CAM-BL3YP[11] functional, the def2-SVP basis set, in CPCM[12] CH2Cl2 as solvent and using the empirical dispersion correction D3-BJ. Approximation of the resolution identity for Coulomb integrals and numerical integration for Hartree-Fock exchange with appropriate auxiliary basis were used as provided by the ORCA software. Absorption transitions were obtained using TDA TD-DFT with the CAM-B3LYP functional along with the PCM CH_2Cl_2 as solvent and with the def2-TZVP basis-

set. Calculation of fraction of transfered electron were performed with an in-house code[13].

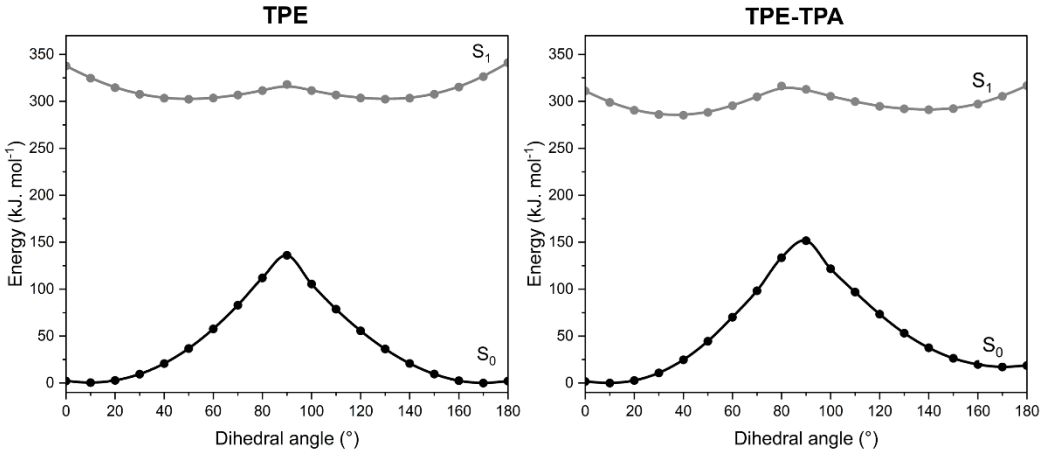

Figure S12: Potential energy surface scan for **TPE** and **TPE-TPA** along the central dihedral angle (TDA-TD)-DFT cam-B3LYP/def2-SVP in CH_2Cl_2(PCM).

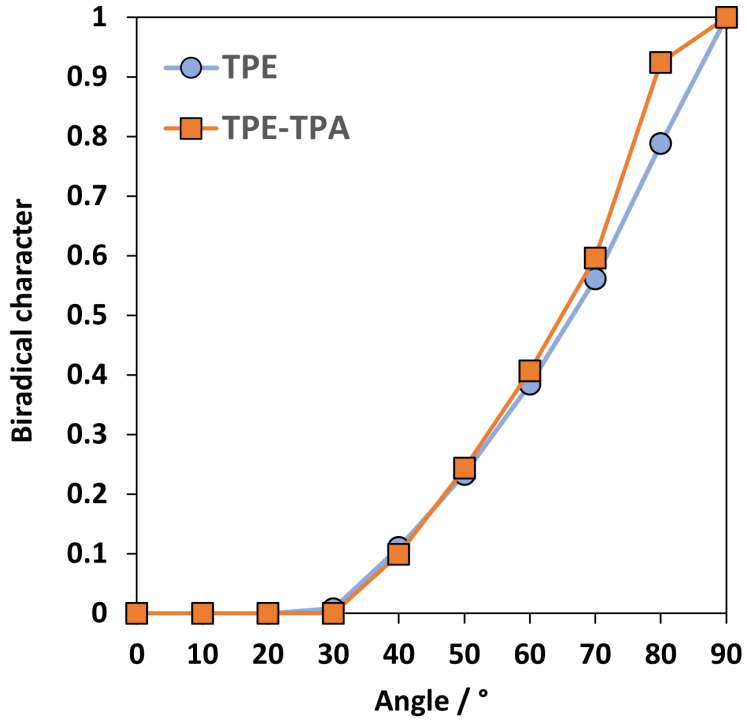

Figure S13: Biradical character of **TPE** (blue curve) or **TPE-TPA** (orange curve) for the optimized S_1 geometry for a given dihedral angle of the central C=C bond.

References

1 J. Rouillon, J. Blahut, M. Jean, M. Albalat, N. Vanthuyne, A. Lesage, L. M. A. Ali, K. Hadj-Kaddour, M. Onofre, M. Gary-Bobo, G. Micouin, A. Banyasz, T. Le Bahers, C. Andraud and C. Monnereau, Two-Photon Absorbing AIEgens: Influence of Stereoconfiguration on Their Crystallinity and Spectroscopic Properties and Applications in Bioimaging, *ACS Appl. Mater. Interfaces*, 2020, **12**, 55157–55168.

2 J. Rouillon, C. Arnoux and C. Monnereau, Determination of Photoinduced Radical Generation Quantum Efficiencies by Combining Chemical Actinometry and 19F NMR Spectroscopy, *Anal. Chem.*, 2021, **93**, 2926–2932.

3 J. M. Donahue and W. H. Waddell, The Trans → Cis Photoisomerization of Protonated Retinyl Schiff Bases, *Photochem. Photobiol.*, 1984, **40**, 399–401.
4 M. Bayda, G. L. Hug, J. Lukaszewicz, M. Majchrzak, B. Marciniec and B. Marciniak, Kinetics of reversible photoisomerization: determination of the primary quantum yields for the E–Z photoisomerization of silylenephenylenevinylene derivatives, *Photochem. Photobiol. Sci.*, 2009, **8**, 1667–1675.
5 C.-J. Zhang, G. Feng, S. Xu, Z. Zhu, X. Lu, J. Wu and B. Liu, Structure-Dependent cis/trans Isomerization of Tetraphenylethene Derivatives: Consequences for Aggregation-Induced Emission, *Angew. Chem. Int. Ed.*, 2016, **55**, 6192–6196.
6 W.-H. Yu, C. Chen, P. Hu, B.-Q. Wang, C. Redshaw and K.-Q. Zhao, Tetraphenylethene–triphenylene oligomers with an aggregation-induced emission effect and discotic columnar mesophase, *RSC Adv.*, 2013, **3**, 14099–14105.
7 J. Wang, J. Mei, R. Hu, J. Z. Sun, A. Qin and B. Z. Tang, Click Synthesis, Aggregation-Induced Emission, E/Z Isomerization, Self-Organization, and Multiple Chromisms of Pure Stereoisomers of a Tetraphenylethene-Cored Luminogen, *J. Am. Chem. Soc.*, 2012, **134**, 9956–9966.
8 K. Kokado, T. Machida, T. Iwasa, T. Taketsugu and K. Sada, Twist of C═C Bond Plays a Crucial Role in the Quenching of AIE-Active Tetraphenylethene Derivatives in Solution, *J. Phys. Chem. C*, 2018, **122**, 245–251.
9 Z. Wang, X. Cheng, A. Qin, H. Zhang, J. Z. Sun and B. Z. Tang, Multiple Stimuli Responses of Stereo-Isomers of AIE-Active Ethynylene-Bridged and Pyridyl-Modified Tetraphenylethene, *J. Phys. Chem. B*, 2018, **122**, 2165–2176.
10 F. Neese, Software update: The ORCA program system—Version 5.0, *WIREs Comput. Mol. Sci.*, 2022, **12**, e1606.
11 T. Yanai, D. P. Tew and N. C. Handy, A new hybrid exchange–correlation functional using the Coulomb-attenuating method (CAM-B3LYP), *Chem. Phys. Lett.*, 2004, **393**, 51–57.
12 M. Garcia-Ratés and F. Neese, Effect of the Solute Cavity on the Solvation Energy and its Derivatives within the Framework of the Gaussian Charge Scheme, *J. Comput. Chem.*, 2020, **41**, 922–939.
13 R. B. Rullan, S. N. Steinmann and T. Le Bahers, Assessing Nonperiodic and Periodic TD-DFT: The Case of Photochromism in Aluminosilicates, *J. Phys. Chem. C*, 2025, **129**, 13051–13063.
14 J. Briand, O. Bräm, J. Réhault, J. Léonard, A. Cannizzo, M. Chergui, V. Zanirato, M. Olivucci, J. Helbing and S. Haacke, Coherent ultrafast torsional motion and isomerization of a biomimetic dipolar photoswitch, *Phys. Chem. Chem. Phys.*, 2010, **12**, 3178–3187.
15 J. Léonard, T. Gelot, K. Torgasin and S. Haacke, Ultrafast fluorescence spectroscopy of biologically relevant chromophores using type II difference frequency generation, *J. Phys. Conf. Ser.*, 2011, **277**, 012017.
16 M. Kurucz, I. Nikolinakos, J. Soueiti, T. Baron, F. Grifoni, W. Naim, Y. Pellegrin, F. Sauvage, F. Odobel and S. Haacke, Transparent Near-IR Dye-Sensitized Solar Cells: Ultrafast Spectroscopy Reveals the Effects of Driving Force and Dye Aggregation, *ChemPhotoChem*, 2024, **8**, e202300175.
17 M. Gerecke, G. Bierhance, M. Gutmann, N. P. Ernsting and A. Rosspeintner, Femtosecond broadband fluorescence upconversion spectroscopy: Spectral coverage versus efficiency, *Rev. Sci. Instrum.*, 2016, **87**, 053115.
18 G. H. Golub and V. Pereyra, The Differentiation of Pseudo-Inverses and Nonlinear Least Squares Problems Whose Variables Separate, *SIAM J. Numer. Anal.*, 1973, **10**, 413–432.
19 D. P. O'Leary and B. W. Rust, Variable projection for nonlinear least squares problems, *Comput. Optim. Appl.*, 2013, **54**, 579–593.